Ammonia Borane Assisted Mechanochemical Boost of Electrochemical Performance of Basal Planes of MoS$_2$-Type Materials

Nikola Biliškov[a,b], Igor Milanović[a,c], Miloš Milović[d], Viktor Takáts[e], Zoltán Erdélyi[f]

[a]*Ruđer Bošković Institute, Bijenička c. 54, 10000, Zagreb, Croatia*
[b]*McGill University, Department of Chemistry, 801 Sherbrooke St W, Montreal, Canada*
[c]*Vinča Institute of Nuclear Sciences, University of Belgrade, Belgrade, Serbia*
[d]*Institute of Technical Sciences of SASA, Belgrade, country{Serbia}*
[e]*Institute for Nuclear Research, Debrecen, Hungary*
[f]*Department of Solid-State Physics, Faculty of Sciences and Technology, University of Debrecen, P.O. Box 400, H-4002, Debrecen, Hungary*

Abstract

The maximization of the number of exposed edges of layered MoS$_2$-type transition metal dichalcogenides of general formula MX$_2$ (M = Mo, W; X = S, Se) is difficult yet meaningful way to improve their electrochemical and electrocatalytic performance. In this work, an all-solid ball milling method for simultaneous introduction of defects and their hybridization through binding of ammonia borane (NH$_3$BH$_3$) to defect sites of MX$_2$ is demonstrated. The milling conditions leads to partial separation and nanosizing of MX$_2$ layers, simultaneously extensively introducing defects (cracks, vacancies, strains, voids etc.), while the detailed analysis revealed the functionalization of the material by binding of NH$_3$BH$_3$ to defect sites, which results in highly improved electrocatalytic performance of thus obtained composites with respect to MX$_2$ for hydrogen evolution reaction. The mechanochemical approach thus enables preparation of MoS$_2$-type materials with improved, highly tunable activity, potentially relevant for energy conversion and storage.

Introduction

Layered structure and highly tunable electronic properties make the MoS$_2$-type transition metal dichalcogenides (TMDC) recently recognised as promis-

ing materials not only for conversion of solar energy to chemical through hydrogen evolution reaction (HER) by water splitting,[1, 2, 3, 4, 5] but also for nanoelectronics,[6, 7, 8, 9, 10] sensorics,[9, 11, 12, 13, 14] or flexible devices,[15, 16, 17, 18] which altogether drastically broadened their applicability far beyond their traditional use as solid lubricants.[19] Their reactivity and electrochemical performance is determined by concentration of edge sites exposed to surrounding medium, while the basal planes are inactive.[20, 21] Thus, it is highly beneficiary to construct single- or few-layered material with a maximized number of exposed edges, which is usually achieved by exfoliation (top-down approach), or by controlled growth of TMDC on carriers (bottom-up approach). Reduction of dimensionality of TMDCs from bulk to their few- or single-layered forms also results in bandgap transformation from indirect to direct, suitable for targeted electronic applications.[22, 23]

Usually, larger amounts of TMDC layers are exfoliated from suspension, most often in organic solvents,[24, 25, 26, 27] although a few examples of sonication of water suspension were described.[28, 29, 30, 31, 32] All of these techniques require extensive use of solvents, which can intercalate between individual layers of 2D materials, thus affecting their properties. On the other hand, classical examples of maximization of the concentration of exposed edges of TMDCs by bottom-up growth comprises bringing the MoS_2 sheets into vertical alignment[33, 21, 34] or building of column-like superstructures.[35]

Introduction of S-vacancies and strain to MoS_2 leads to hydrogen absorption free energy close to $\Delta G_H = 0 \, \text{kJ} \, \text{mol}^{-1}$,[36, 37, 38, 39, 40] and thus HER activity comparable to platinum.[20, 41] This implies that electrochemical performance of TMDCs can be improved by intentional introduction of defects to basal planes, i.e. chalcogenide- or metal-vacancies, cracks, voids etc. Ball milling comprises a simple and efficient means of crushing the material, but more important in this context is that continuous striking of the material in the process of ball milling causes a simultaneous amorphisation and introduction of a large number of defects in the form of cracks, crevices and other breakdowns, thus should result in nanosized sheets with large number of exposed edges.[42] For this reasons, ball milling potentially represents a simple and scalable method for production of layered, edge-rich 2D-materials.[43, 44] Ball milling enables not only physical, but also chemical transformation, induced by mechanical energy, transferred from milling device to solid chemical system.[45, 46] Thus, this method opens new possibilities for simple and efficient green preparational procedures toward advanced

2

hybrid 2D materials,[47, 48, 32, 49] in this case by hybridization of vacancies.

In the present study we explore the influence of milling-induced edges and defect sites and their hybridization by ammonia borane (NH_3BH_3, further in the text ABH) to electrochemical performance of transition metal dichalcogenides of general composition MX_2 (M = Mo, W; X = S, Se). ABH has attracted a considerable attention as a potential material for solid-state hydrogen storage.[50, 51, 52] Its unique chemistry arises from coordination bond between ammonia NH_3 and borane BH_3 moiety, as well as the presence of hydrogen in two different forms: protic H atoms of NH_3 and hydridic H atoms of BH_3, giving rise to dihydrogen bonding of $NH^{\delta+}\cdots H^{\delta-}B$ type. This makes ABH a stable crystalline solid in ambient conditions. Here, ABH is a source of boron atoms, which could bridge the mechanically produced X-vacancies and in this way lead to theoretically predicted composites of significantly improved electrochemical and catalytic performance.[53] Potentially, individual or combined action of all the above discussed effects could result in novel, highly efficient TMDC-based semiconductive materials for energy conversion and storage.[54]

1. Experimental details

1.1. Materials

Molybdenum(IV) sulfide MoS_2 (99 %), molybdenum(IV) selenide $MoSe_2$ (99.9 %) and tungsten(IV) sulfide WS_2 (99.8 %) were purchased from Alfa Aesar, while ammonia borane NH_3BH_3 (97 %, further in the text ABH) was purchased from Boron Specialties. Tungsten(IV) selenide WSe_2 was prepared by overnight heating of tungsten (Koch Light Labs, 99.99 %) with stoichiometric amount of selenium (Alfa Aesar, $2-5$ mm shots, 99.999 %) at 900 °C in evacuated quartz tube.

Throughout the text, we use the notation as follows: transition metal dichalcogenides are denoted as TMDC, ammonia borane NH_3BH_3 is denoted as ABH, general composition MX_2 (M = Mo, W; X = S, Se or Te) is denoted as MX2, while MX_2 + ABH systems are denoted as MX2-ABH. Specific systems are denoted by using a combination of formula unit with ABH, for example MoS_2-ABH for MoS_2-ABH.

For all preparations, a Spex 8000M mill-shaker was used. Milling frequency was 875 cycles per minute in a number eight-shape motion, and the applied milling time was 30 min. In all preparations, the mass of reaction

mixture was $\approx 250\,\mathrm{mg}$. In-house designed gas-tight mechanochemical jars (ESI, Fig. S1) were used, with stainless steel ball $m = 4\,\mathrm{g}$.

To ensure inert atmosphere during the milling of the samples, all manipulations were conducted in an argon-filled Labmaster 130 MBRAUN glovebox (< 0.1 ppm O_2 and < 0.1 ppm H_2O). More details on preparation of the samples and exfoliation experiments are given in ESI, sections S1.1 and S1.2.

1.2. Characterization

Detailed description of characterization procedures is given in ESI, section S1.3.

X-ray powder diffraction (PXRD) patterns were recorded using a Panalytical Aeris system with CuKα radiation ($\lambda = 1.5418\,\text{Å}$). The 2Θ range was $5 - 70°$ with a $\Delta(2\Theta) = 0.0221°$ step and counting time per step was $0.25\,\mathrm{s}$.

Infrared (IR) spectra in ATR mode are measureed by a ABB Bomem MB102 FTIR spectrometer with DTGS detector and CsI optics, equipped with a Specac Golden Gate single-reflection ATR accessory with IIIA type diamond trigonal prism shaped ATR element metal-bonded into a tungsten carbide mount. The angle of incidence is $45°$. This optical assembly enables acquisition of IR spectra in $4000 - 450\,\mathrm{cm^{-1}}$ range. Each spectrum represents an average of 10 co-added Fourier-transformed interferograms (scans). The nominal resolution is $4\,\mathrm{cm^{-1}}$ which gives a distance between two points in the resulting spectrum $2\,\mathrm{cm^{-1}}$.

Temperature-dependant IR spectra are acquired in transmission mode, using KBr pellets ($\sim 100\,\mathrm{mg}$ KBr $:\sim 1\,\mathrm{mg}$ sample). The controlled heating of the samples was allowed by use of Specac's high-stability temperature controller. The samples were continuously heated from room temperature to $250\,°\mathrm{C}$ at a heating rate $5\,°\mathrm{C\,min^{-1}}$, and the spectra were acquired at a $5\,°\mathrm{C}$ step. Spectral resolution was set to $4\,\mathrm{cm^{-1}}$, and each spectrum represents an average of 5 co-added Fourier-transformed interferograms (scans), which took $10\,\mathrm{s}$ per spectrum, implying temperature accuracy of $\pm 1\,°\mathrm{C}$.

Thermogravimetric analysis coupled with quadrupole mass spectroscopy (QMS-TG) was done using a Netzsch STA 449F5 instrument. $85\,\mathrm{\mu L}$ Al_2O_3 crucibles with drilled lids were used as sample holders. Heating rate was set to $5\,°\mathrm{C\,min^{-1}}$. N_2 was used for both purging ($20\,\mathrm{mL\,min^{-1}}$) and protective gas ($50\,\mathrm{mL\,min^{-1}}$). The measurements were done over a $35 - 700\,°\mathrm{C}$ temperature range. Gaseeous products over $1 - 100\,\mathrm{au}$ mass range were measured by a QMS coupled to TG through a $2\,\mathrm{m}$ long capillary tube heated to $250\,°\mathrm{C}$ to prevent condensation.

Particle size distribution was measured by dynamic light scattering (DLS), using a Malvern Zetasizer Nano ZS, which measures ζ-potential in liquid dispersions, in the hydrodinamic size range between 0.6 nm and 6 µm. Samples were dispersed by sonication over 30 min in petroleum ether as liquid matrix.

Scanning electron microscope (SEM) with energy dispersive X-ray spectroscopy (EDS) measurements were done using a FEG Quanta 250 SEM FEI and a Jeol 7000 FE-SEM instrument.

X-ray photoelectron spectra (XPS) were measured using a Specs XPS instrument fitted with an XR-50 dual anode X-ray source (150 W (14 kV) Al K_α anode) and a Phoibos 150 energy analyzer. The powdered samples were pressed onto an indium foil for mounting. The spectra were acquired with a step size of 0.1 eV and a pass energy of 20 eV with 25 scans. For assignment of the XPS peaks we used NIST XPS database.[55]

1.3. Electrochemical measurements

The electrocatalytic activity of the prepared both pristine and mechanochemically treated samples has been measured by linear sweep voltammetry (LSV), using an Ivium Vertex.One potentiostate/galvanostate. The measurements have been carried out in the conventional three-electrode cell setup with aqueous solution of H_2SO_4 as electrolyte ($c = 1\,\mathrm{mol\,dm^{-3}}$). Graphite plate and SCE (saturated calomel electrode, SI Analytics) were used as counter and reference electrode, respectively. Working electrode consisted of the active material and polyvinylidene-difluoride (PVDF, Sigma-Aldrich) mixed in 95 : 5 wt. ratio and deposited on a glassy carbon plate from the slurry prepared in N-methyl-2-pyrrolidone (Sigma-Aldrich, 99 %). Scan rate was set to $5\,\mathrm{mV\,s^{-1}}$.

Results and discussion

Before any experimentatal work with TMDCs, the ABH-assisted mechanical exfoliation of graphite[56] was repeated here in order to check if the results obtained by planetary mill are comparable to those obtained by using a mill-shaker. Indeed, a 3 h milling of 1 : 2 mixture of ABH and graphite resulted in a product with the Raman spectrum, PXRD and SEM images equal to the results reported earlier (Fig. S2).[56] Having in mind that the 8-shaped movement of mill-shaker effectively combines shear forces with impacts, it is indicated that the exfoliation of graphite is dominated by mechanically

assisted intercalation of ABH between individual graphene sheets, which reduces the interlayer force, thus assisting their separation. Raman spectra and PXRD show that the most successful intercalation of ABH was achieved for the (graphite : ABH) = 1 : 2.7 molar ratio (Fig. S2). Analogously, MX2 were milled with excess ABH (Table S1).

PXRD patterns of pristine TMDCs are dominated by the (002) reflection, corresponding to the interlayer separation along the c-axis (Fig. S3), dominantly defined by ionic radius of the chalcogenide atom. As the applied mechanical force causes separation of individual layers, correlations along the crystallographic c-axis disappear, causing a decrease of the intensity of $(00l)$ reflections, while the correlations within the layer remain intact, as reflected in constant $(hk0)$ intensities. Thus, milling of the samples causes a significant drop of intensity of the (002) reflection (Fig. 1), confirming a loss of interlayer ordering. Additionally, this line is highly broadened (Fig. 1), which indicates a decrease of the average crystallographic size along the c-axis, i.e. orthogonal to the basal plane of the layer, due to mechanically induced amorphisation. The crystallite thickness after the ball milling treatment, as determined by Scherrer analysis of (002) reflection, (Fig. S14) ranges between $35 - 100\,\mathrm{nm}$ with a narrow distribution for all considered MX2. With an interlayer distance of $\sim 0.3\,\mathrm{nm}$, this corresponds to $\sim 50 - 170$ layers.

The decrease of (002) line and its broadening is partially suppressed by addition of ABH. Concretely, the widths of these lines remain approximately $4\times$ narrower for MX2-ABH systems (Fig. 1), and the Scherrer analysis of the (110) reflection shows that after milling the crystallite lateral size ranges between $100 - 250\,\mathrm{nm}$, i.e. $\sim 160 - 415$ layers. Thus, although the milling evidently leads to decrease of crystallite size, the samples are not exfoliated, which clearly indicates that the treatment of TMDCs with ABH by means of ball milling induces significantly different processes and thus different outcome with respect to graphite case.

A sharp decrease of integral intensity of ABH-related PXRD lines in the initial phase of milling indicates its efficient and instant interaction with MX2 matrix, competing with exfoliation of TMDC sheets, which is strongly dependent on chalcogenide atom of the MX2 (Fig. 1). SEM-EDS (Figs. 2, Figs. S19-S21 and Table S5) shows a complete coverage of MX2 by ABH, with a significant nitrogen deficiency in all cases, which is especially pronounced in regions with a thinner ABH crust, where the MX2 species become visible to EDS. Additionally, a $10\,\%$ deficiency of chalcogenide atoms with respect of the MX_2 formula is observed, which is attributed to formation of X-vacancies
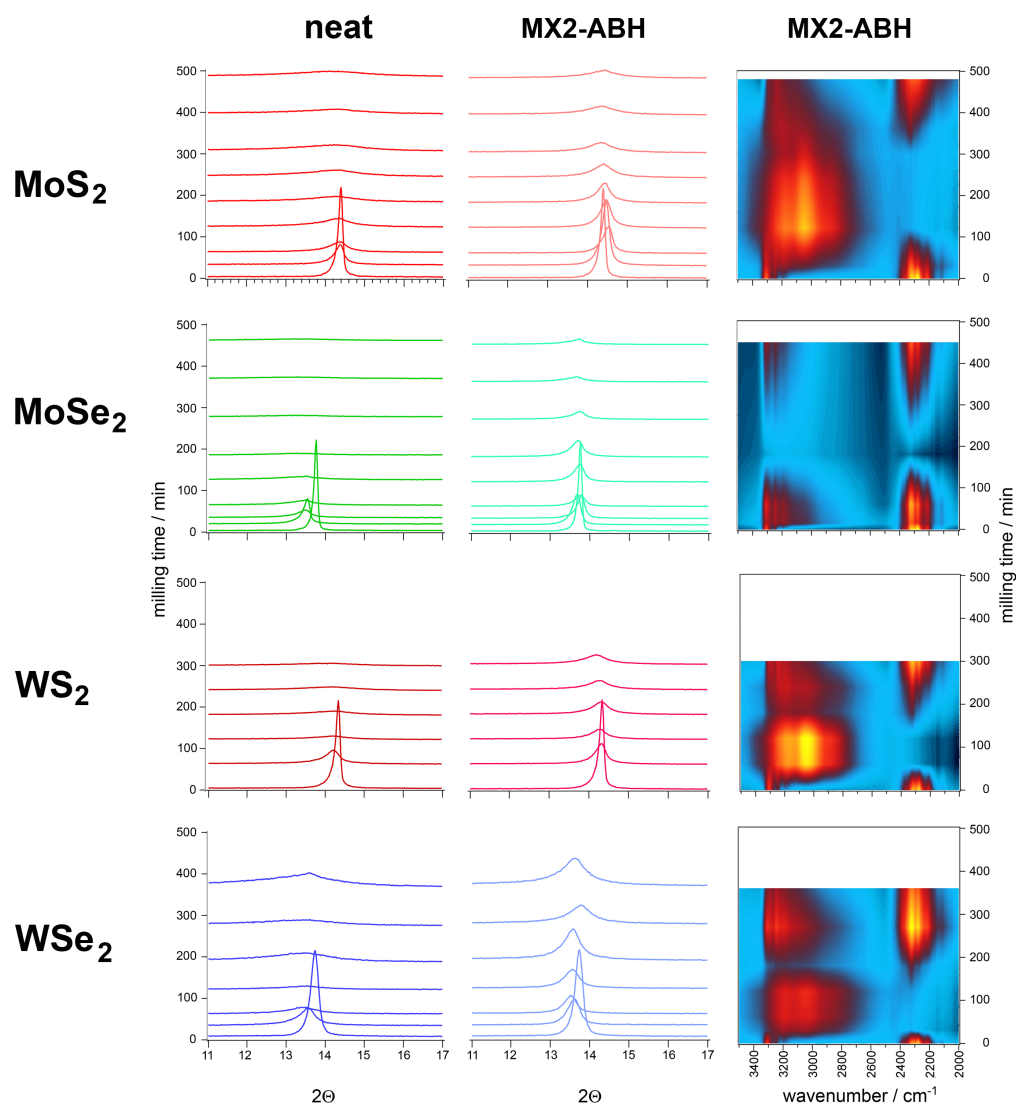
Figure 1: Comparison of the milling time-dependant behaviour of (002) line of PXRD for MX2 and MX2-ABH with changes in IR spectra for MX2-ABH systems.

in the structure of MX2 systems, then occupied and bridged by BH_3 moieties of ABH,[53] while chalcogenide atoms are hydrogen bonded to NH_3 groups of ABH. This way, ABH acts as a bifunctional separator of TMDCs, that is chemisorbed to the edges and cracks, as well as X-vacancies of MX_2, and the exfoliated nanosheets thus survive harsh high-energy milling conditions. This is apparently in contradiction with IR spectra (Fig. S16), For instance, IR spectrum of WSe2-ABH-60 shows the absence of $\nu(BH)$, while $\nu()$ remains very broad indicating hydrogen bonding. Conclusively, combined results from IR and EDS indicate a milling-induced release of NH_3, while the rest of NH_3 groups of ABH remain hydrogen bonded in the system. The release of NH_3 was tested by Cu^{2+} complexation test (described in ESI, section S1.3), which resulted in characteristic change of color to dark blue upon opening of the milling jar.

Due to inherent methodological harshness, ball milling leads to laterally smaller crystallites, irrespective of the initial size in the bulk phase, in comparison with redox [57] or liquid phase exfoliation (LPE) technique.[25] Indeed, particle and crystallite size analysis shows no quantitative regularity in prepared materials. Tribological studies of mechanochemical processes show that the system tends to decrease its bulk coefficient of friction.[58] On the other hand, molecular dynamics simulations suggest that a considearable exchange of chalcogenide atoms takes place in these conditions.[59] Thus formed X-vacancies act as reactive sites, which readily react with ABH or other defect sites available in neighbouring layers. These processes supress the exfoliation, pushing the systen toward more complex composites. It is interesting to note at this point that the size of the produced grains is irrespective on the system, and it is determined exclusively by the internal conditions inside the milling vessel. However, MX2-ABH crystallites remain larger with respect of corresponding MX2. Altogether, these observations and previously published studies suggest a healing effect of ABH, similar to that observed in the case of $NH_3 + MoS_2$ system[60] or theoretically predicted bridging of X-vacancies by boron atoms[53] with simultaneous transfer of chalcogenide atoms from MX_2 defect sites to ABH.

IR spectra of MX2-ABH systems are dominated by absorption bands due to ABH, which makes IR spectroscopy a good probe of its interaction with MX2. For the purposes of this study it is sufficient to focus on stretching bands, namely $\nu(NH)$ in the $3500 - 3000\,cm^{-1}$ range, $\nu(BH)$ in the $2500 - 2000\,cm^{-1}$ range and $\nu(BN)$ present at $780\,cm^{-1}$ for neat ABH.[50] IR spectra (Fig. 1) show that milling causes a disappearance of $\nu(BH)$ and $\nu(NH)$
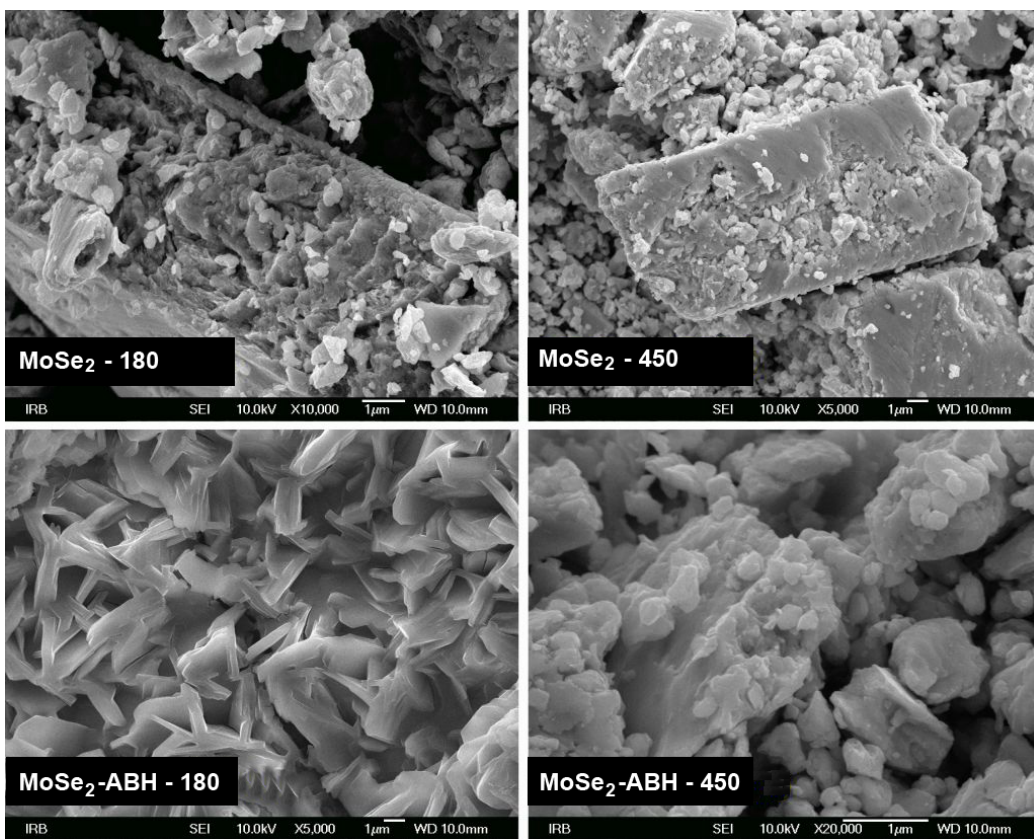
Figure 2: SEM images of the milled samples of $MoSe_2$ and $MoSe_2 + ABH$. 180 and 450 refer to applied milling time in min.

features for all investigated MX2-ABH systems, and the process depends on the metal atom of the MX2. For Mo-containing systems, this feature disappears after $\sim 120\,\text{min}$ of milling, and reappears after $\sim 360\,\text{min}$. For W-containing systems, it readily disappears after $\sim 30\,\text{min}$, and reappears after $\sim 180\,\text{min}$. Simultaneously with disappearance of $\nu(\text{NH})$ and $\nu(\text{BH})$, the appearance of a very broad feature in the $3200 - 2600\,\text{cm}^{-1}$ region is evident (Fig. 1 and S16). The feature is more intense for S-containing systems. This feature indicates the formation of strong hydrogen bonds between NH_3 group of ABH with chalcogenide atoms of the MX2, especially with S. Additionally, for all systems the $\nu(\text{BN})$ band is intensified and shifted from 780 to 808 and $802\,\text{cm}^{-1}$ for MoX_2 and WX_2, respectively (Fig. S17), which indicates a strengthening and increase of polarisation of the coordination B-N bond, caused by perturbated electron density upon binding of B atoms of ABH to Mo or W. The reappearance of $\nu(\text{NH})$ and $\nu(\text{BH})$ envelopes by prolonged milling is caused by an interaction of ABH through boron with both metal and chalcogenide atom, leading to disruption of containing $\text{NH}_3\cdots\text{X}$ hydrogen bonding network, which is explained in more details further in the text.

In line with this, the position of (002) line of MX systems is greatly affected at the beginning of milling, and this behaviour is mainly determined by chalcogenide atoms (Fig. 1). The evolution of (002) line position clearly shows that sulfides are relatively persistent in the milling conditions, while selenides suffer more evident (002) shifts, and thus significant change in c parameter, while a remains mainly intact (Figs. S9 and S10). This indicates a partial or complete separation of layers during the milling. Indeed, the evidence from PXRD shows that pristine sulfides and selenides persist in 2H phase during the whole ball milling process. Addition of ABH to MX2 systematically decreases the line shift, but the difference between the systems with the same chalcogenide atoms are somewhat more pronounced (Fig. 1). The crystallite size is sharply reduced during the first phase of milling, and it is practically not affected by addition of ABH.

The width of the PXRD lines for MX2-ABH systems remains relatively intact with respect of pristine MXs by milling, indicating the preservation of crystalinity. Additionally, milling of the MX2-ABH leads to somewhat thicker ($\tau_{002} \approx 10\,\text{nm}$) crystallites and larger crystallite flakes (lateral size $\tau_{110} \approx 300\,\text{nm}$) with respect to MX2. These observations indicate a structural ordering through an interaction between ABH and MX2 (Fig. 4). A prolonged milling leads to thicker MX2-ABH particles. It is previously observed that the MX2 systems tend to self-heal the structural impact-induced defor-

mations by chemisorption of NH_3 by edge and deformation-exposed chalcogenide atoms.[60] The sytructure can be additionally stabilized by boron atoms bridging X-vacancies through covalent binding to metal atoms, additionally stabilizing the structure.[53]

To probe the hypothesized occupancy of MX_2 defect sites by ABH, B(1s) core level XPS spectra were collected for MX2-ABH systems milled for 15, 180 and 450 min, respectively (Fig. 3). The signals attributed to B-N bonding are irregular with respect of the milling time, which indicates high disorder of the systems. However, a series of signals and their behaviour indicate the formation of B-M and B-X bonds, respectively. The 190.5 eV signal is common for molybdenum-containing systems, while tungsten-containing systems give rise to 190.7 eV signal. The intensities of these signals evidently increase with milling time, indicating milling-induced formation of B-Mo and, more prominently, B-W bonds. On the other hand, 189.4 eV signal indicates formation of B-S bonds, while the 189.8 eV signal is attributed to B-Se. However, these two signals show significant difference in their behaviour. While the B-S signal increases with milling time, the B-Se shows significant drop of intensity after 180 min, indicating a further rearrangements in these systems. The presence and common behaviour of these signals indicate the occupancy of impact-induced cracks and voids in MX2 structures by boron atom of ABH through covalent bonding. Unfortunately, the N(1s) XPS results were very unreliable, with very poor S/N ratio. As shown by EDS analysis (Table S5), the N content is very low for all the MX2-ABH systems.

A combined information obtained from IR and XPS spectra clearly reflect covalent binding of boron to metal and chalcogenide atoms, which is especially valid for W-containing systems (Fig. 3) at milling-induced deformations of the MX_2 matrix. Interaction of ABH with chalcogenides causes strengthening and thus further stabilization of strongly bind $NH_3BH_3 \cdots H_3NBH_3$ network, which is reflected in formation of very broad IR envelope in the $3600 - 2500 \, cm^{-1}$ region and blue shift of $\nu(BN)$ band (Figs. S16 and S17). The shape and locations of maxima of the envelope is independent on MX2, indicating that this interaction is not directly affected by MX2. However, it is disrupted by prolonged milling, when at the defect sites B-M bonds become predominant (Fig. 3). It is evident from thermodynamic consideration that the tungsten borides are generally more stable with respect of molybdenum borides,[61] which explains the trend of the B-M XPS signal, as well as the behaviour of IR spectra for W- with respect to Mo-containing systems. The reactive molecular dynamics simulations show that the tribochemical
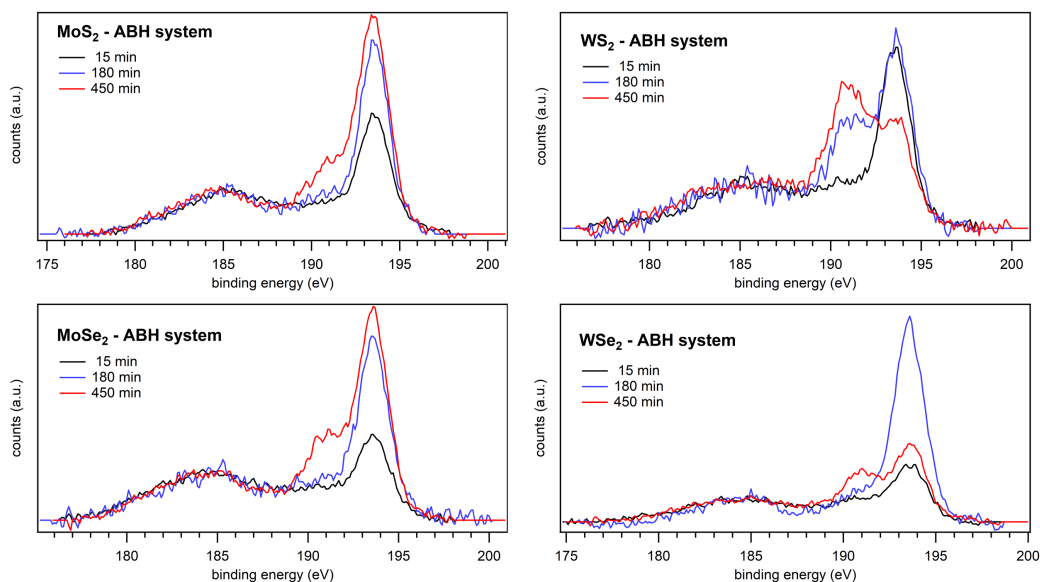
11

Figure 3: B(1s) XPS spectra of the MX2-ABH samples with respect of the milling time.
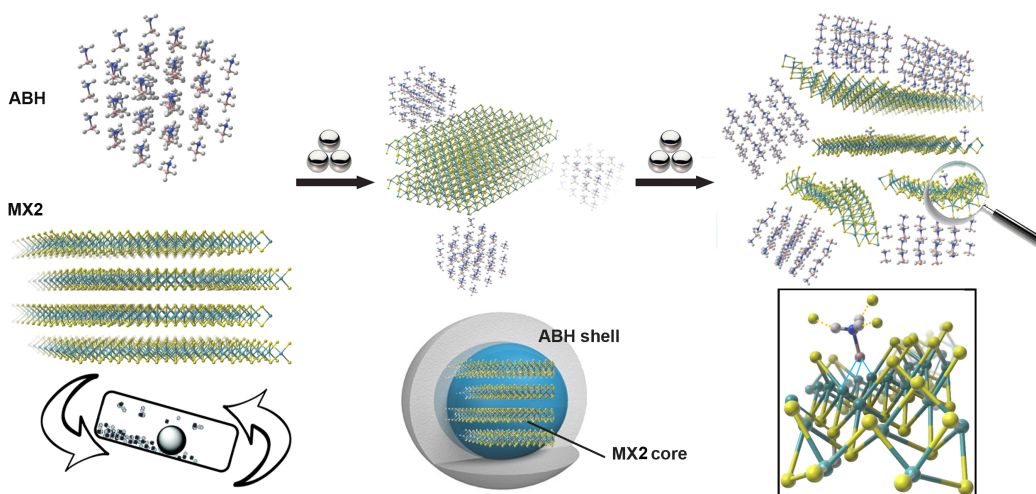

Figure 4: During the first stages of milling (movement of the here applied milling jar schematically shown), multi-layered blocks of MX2 are surrounded by ABH, building a MX-core - ABH-shell structure, which is stabilised by binding of B to milling-introduced defect sites, i.e. X-deficient M atoms. This is enforced by strong $NH^{\delta+}\cdots H^{\delta-}B$ dihydrogen bonding and $NH\cdots X$ hydrogen bonding. This promotes binding of $BH^{\delta-}$ to X-deficient M sites. Prolonged milling causes untying of $BH\cdots M$ interaction, leading to domination of ABH ordering around MX2 through $NH_3BH_3\cdots H_3NBH_3$ dihydrogen bonding.

12

conditions cause rearrangements of bonding patterns involving chalcogenide atoms,[59] which should be investigated for the case of MX$_2$-ABH systems.

A prolonged milling causes separation of ν(NH) and ν(BH) envelopes in IR spectra (Fig. 1), while XPS spectra (Fig. 3) show further increase of M-B, while B-X signals drop for all systems. This indicates that interaction of ABH through boron with both metal and chalcogenide atoms causes extensive changes in hydrogen bonding network. SEM shows that the morphology is significantly altered (Fig. 2), while EDS indicates a 10 % deficiency of chalcogenide atoms.

These observations altogether indicate that formation of strong hydrogen-bonded NH···X species causes a decrease in initial ordering of ABH, with preservance of the MX2 ordering. SEM/EDS shows a complete coverage of MX2 particles by ABH (Fig. 2), which preserves MX2 structure from amorphisation by building core-shell structure consisting of a tight hydrogen bonded crust of ABH around MX2. EDS measurements also indicate a significant N- and X-deficiency for samples after prolonged milling, especially in the regions covered by tinier ABH crust, where the N-deficiency is 2× higher with respect to regions with thicker ABH. This indicates that inner shells of adsorbed ABH mainly contributes the observed N- and X-deficiency, while the outer shell is built from ABH molecules in interaction with those directly bound to MX2, in accordance with abovementioned hypothesis of formation of B-functionalised X-vacancies. Indeed, the previously published DFT calculations show that from such B-functionalised MX2 systems NH$_3$ release is a preferred process,[53] which further promotes B-X bonding. Thus, in the first phase of milling hydrogen bonded ABH crust covers the surface of MX2, forming a core-shell structure. However, different from adsorption to graphite,[56] ABH strongly interacts with MX2, and simultaneously a strong dihydrogen bonding of the B$-$H$^{\delta-}$····H$^{\delta+}-$N type was formed on the exposed sites, resulting in transfer of hydridic H B····H$^{\delta-}-$H$^{\delta+}-$N with release of some amount of NH$_3$,[53] which is evident for MoS$_2-$ABH system (Fig. S23). Previously observed adsorption of NH$_3$ with MoS$_2$ and WS$_2$ indicates its realisation through an interaction of lone electron pair of NH$_3$.[62, 63] In the case of ABH, this points to preferred interaction of BH$_3$ groups with MX$_2$ surface, which sticks the layers together (Fig. 4).

The extensive relatively strong interaction of ABH with MX2 prevents their exfoliation by formation of stable composite. This process preserves the structural ordering, witch starts when the concentration of ABH on the surface of MX2 or interlayers reaches a critical concentration, namely when
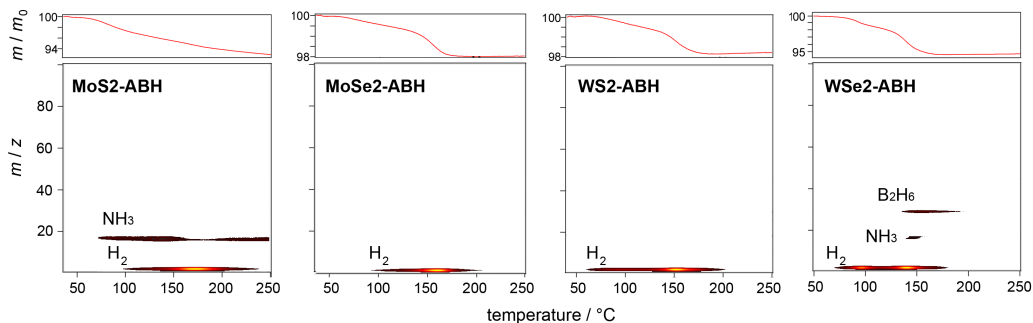
Figure 5: QMS-TG measurements of the MX2-ABH systems.

ABH molecules start to build mutual dihydrogen bonded network similar to those in neat ABH. The robustness of the intercalated structure is reflected in observation that IR spectra and XRD patterns of MX2-ABH systems remain practically intact even after 6 months, as well as after exposure to high vacuum or after the treatment with EtOH (dispersion, sonication and washing). Thus, the intercallated ABH holds the MX2 sheets sticked together even after a prolonged milling. Simultaneously, they are attracted to each other by electrostatic attraction of opposite charged hydrogen atoms, through formation of dihydrogen bonded pairs, characteristic to neat ABH, leading to preservation of crystalinity of MX2-ABH.

This is further supported by comparative TG/DSC-QMS (Fig. 6) and temperature-dependent IR spectroscopy measurements (Fig. 5). Thermal decomposition of ABH is strongly affected by the MX2, and the QMS pattern of H_2 release is significantly different with respect to neat ABH.[50] In the case of Mo-containing MX2-ABH, its decomposition occurs in the $100 - 200\,°C$ region over two dehydrogenation steps. The lower temperature step with a maximum at 128 and $147\,°C$ for MoS_2-ABH and $MoSe_2$-ABH, respectively. This step is very broad and highly overlapped with better defined higher temperature step, peaking at 173 and $160\,°C$. On the other hand, decomposition of ABH in W-containing systems occurs over two well separated main events, similar to that for pristine ABH. However, an additional, significantly weaker step, occuring at $170\,°C$, accompanied by release of a trace amount of NH_3, is also observed. The main dehydrogenation events occur at 105 and $150\,°C$ for WS_2-ABH and at 96 and $140\,°C$ for WSe_2-ABH, reflecting a partial stabilization of ABH by binding to X-vacancies of Mo-containing systems. Additionally, only in the MoS2-ABH case dehydro-
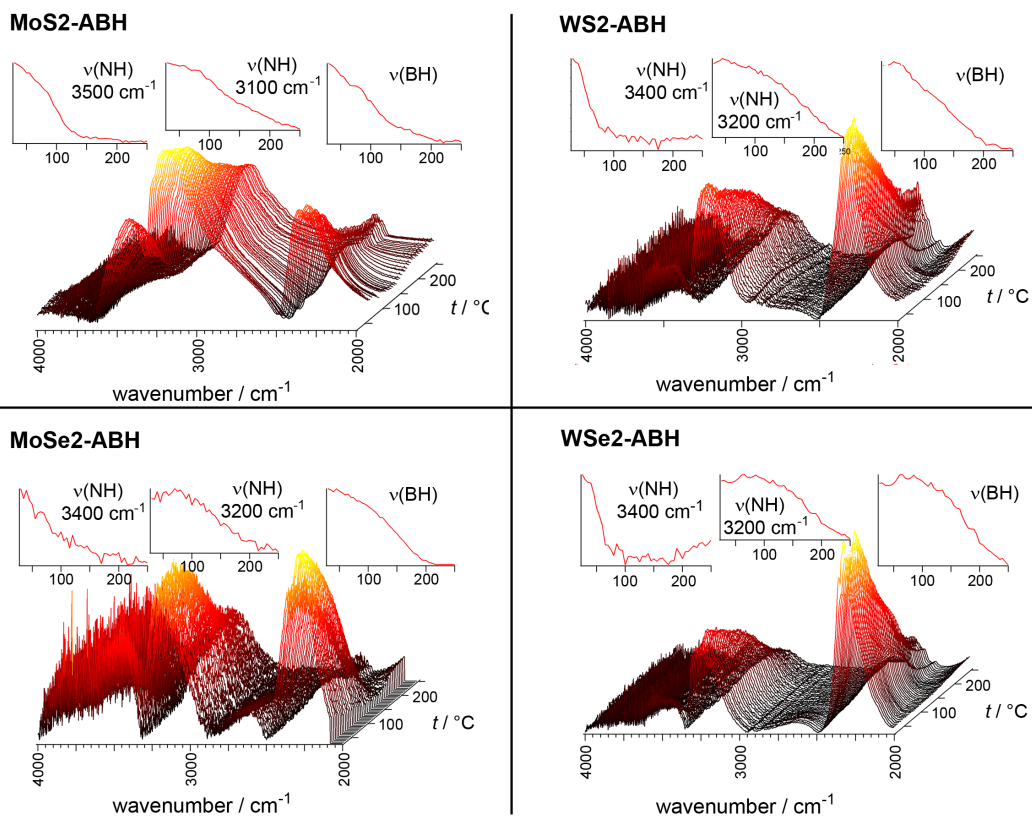
14

MoS2-ABH

ν(NH)
3500 cm⁻¹

ν(NH)
3100 cm⁻¹

ν(BH)

WS2-ABH

ν(NH)
3400 cm⁻¹

ν(NH)
3200 cm⁻¹

ν(BH)

MoSe2-ABH

ν(NH)
3400 cm⁻¹

ν(NH)
3200 cm⁻¹

ν(BH)

WSe2-ABH

ν(NH)
3400 cm⁻¹

ν(NH)
3200 cm⁻¹

ν(BH)

Figure 6: Temperature-dependent IR measurements of the MX2-ABH systems.

15

genation is accompanied by the release of significant amount of NH_3 and trace amount of B_2H_6 for WSe2-ABH (Fig. S23), while the B-N containing species are not detected in any case. Temperature-dependant IR measurements show a faster decrease of the overall intensity of the $\nu(NH)$ stretching envelope with respect to $\nu(BH)$ region (Fig. 5). The absence of NH_3 and B-containing species in QMS signal indicate their chemical reaction with defect sites of the MX2. Previous considerations indicate binding of the B atoms to chalcogenide-deficient Mo or W atoms at milling-induced defect sites of MX2. Although the previously published DFT calculations show that from such B-functionalised TMDC systems NH_3 release is a preferred process,[53] it is not evident from our measurements, indicating the retain of the chemical identity of the products of decomposition of ABH when bound to MX2.

Thermal decomposition of ABH contained in MX2-ABH systems proceeds through formation of conmplex mixture of $-(H_xBNH_y)_n-$ polymeric and oligomeric species, finally leading to BN.[50, 64]

Electrochemical performance of freshly prepared MX2-ABH systems was investigated with respect of their potential use as electrocatalysers for hydrogen evolution reaction (HER). In this reaction, electrons from the external circuit combine with protons at catalytic sites at the interface of electrode and electrolyte, thus forming H_2 through a stepwise process, consisting of binding of H atoms to catalytic site, their recombination to H_2 and, finally, desorption. This is checked by measuring cathodic polarization curves for electrodes prepared from MX2-ABH systems (Fig. 7 (a-b)). From them, the parameters of the Tafel equation are provided in Table S6. As a consequence of prolonged milling, amorphisation and grain size reduction together provide additional active sites, and the onset potential for all tested electrodes shifts toward more positive values, with respect to bulk TMDCs.[65, 66] The observed values are very similar to those obtained in the case of exfoliated reduced TMDC sheets.[67] The only exception is WSe2-ABH system, which shows significantly more positive values of onset potential. Interesting, exfoliation of this system leads to potential similar to the bulk WSe_2,[67, 65] but mechanochemically prepared WSe2-ABH composite is significantly improved with respect to HER.

Tafel slopes are relatively invariant with respect to milling time and thus to crystallite size. It indicates that the proton discharge reaction (Volmer step), i.e. binding of the protons to catalyst active sites:
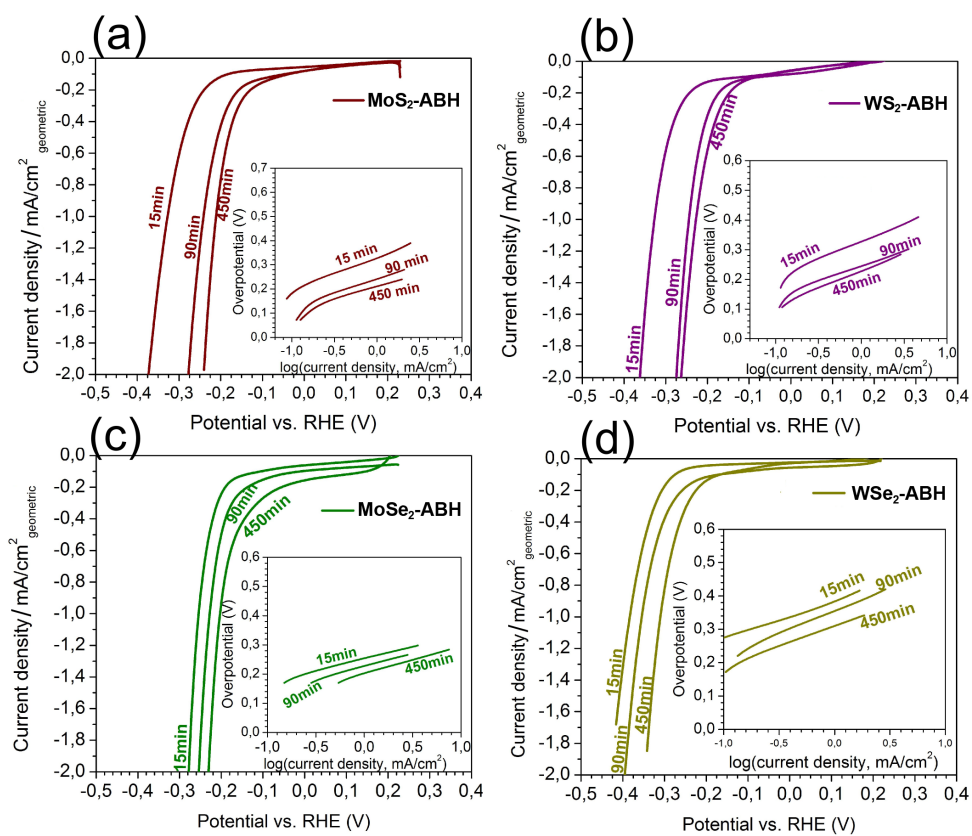
$$H_3O^+ + e^- + \star \underset{\longleftarrow}{\overset{\longrightarrow}{\rightleftharpoons}} H^\star + H_2O$$

16

Figure 7: Polarization curves of tested MX_2 samples mechanically treated (15-450 min) with ammonia borane: (a) MoS_2, (b) WS_2, (c) $MoSe_2$ and (d) WSe_2 and its corresponding Tafel plots (a-d insets).

is rate determining step for all the tested electrodes.[68] However, it is notable that addition of ABH decreases the slope, increasing the Heyrovsky contribution to the HER mechanism, i.e. H_2 desorption:

$$\star + H_3O^+ + e^- \xrightleftharpoons{} H_2 + H_2O + \star$$
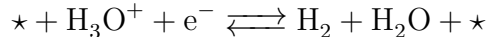
In the other words, mechanochemical hybridization of MX2 with ABH encourages the desorption of H_2, thus promoting the overall HER process. However, this is not significantly improved by prolonged milling.

ABH hybridization of S-containing MX2 systems does not significantly affect their exchange current densities, which are the same order of magnitude as those obtained for nanoparticles loaded on Toray carbon paper ($\sim 4.6 \times 10^{-6}\,\mathrm{Acm^{-2}}$).[66] Thus, ABH improves HER catalytic activity of S-containing MX2 (Fig. 7), as evident by comparison of MX2-ABH composites with pristine MX2 samples prepared under equal conditions (Fig. 7 a-b and Table S6). These observations are direct consequence of the binding of B atoms to S-deficient metal atoms at the milling-induced defect sites (Fig. 1, IR spectra), which forms "islands of stability". However, ABH hybridization of selenides stabilizes the exchange current density, which is in both cases only slightly decreased by milling. They show a less pronounced improvement of HER catalytic activity, as evident from Fig. 7 (c-d). Selenides also show a narrower distribution of polarization curves for different milling times with respect to sulfides (Fig. 7).

The values of potential at constant current density (2.0 mA) $MoSe_2$ system fall in the range from -0.31 to $-0.18\,\mathrm{V}$ for all samples, while for $MoSe_2-ABH$ system distribution of E values at the same current density are in the range from -0.28 to $-0.23\,\mathrm{V}$. The same trend is evident for WSe_2 and WSe_2-ABH with range of potential between -0.60 to $-0.21\,\mathrm{V}$ and -0.43 to $-0.34\,\mathrm{V}$, respectively. Distinct effects of ABH on MX2 are clearly evident in the case of WS_2 and WSe_2 (Figs. S24 and S25). $WS_2 - ABH$ composite improves catalytic activity regardless of milling time. However, in the case of $WSe_2 - ABH$, short milling improves catalytic capabilities of the system, but prolonged milling leads to degradation of its HER catalytic performance.

Conclusions

An obvious consequence of the ball milling treatment of MX2 and MX2-ABH systems is a partial exfoliation accompanied with an extensive introduction of defects to MX2 basal planes. MX2 particles are completely covered by

ABH, organized in form of core-shell structures stabilized by binding of B and N atoms of ABH to M or X, respectively, and by extended hydrogen bonding network between surrounding ABH molecules. MX2 particles are therefore prevented from further decomposition, even in the harsh mechanochemical conditions. Thus, ABH acts as a bifunctional separator of MX2, that is chemisorbed to the edges and cracks, as well as X-vacancies.

Electrochemical properties and activity of investigated MX2-ABH systems follow these compositional changes. During the initial phase of milling with ABH structural blocks of MX2 are cracking and ABH penetrates into their structure, between the layers at edges and defect sites. However, after the initial phase, sulfides are subject to reorganization, which is not observed for selenides. A combined consideration of IR spectra and electrochemical measurements gives a correlation of structure and electrochemical performance of MX2-ABH systems, with respect to their HER activity. MX2-ABH systems with extensive B occupancy of X-vacancies and strong NH···X hydrogen bonds are representing stability windows for investigated electrode materials. Materials without ($MoSe_2-ABH$) and with very narrow (WSe_2-ABH) stability windows show only a modest catalytic activity for HER. However, a more detailed investigation of (photo)electrocatalytic performance of here presented systems and their optimization with respect to HER is required.

Thermal decomposition of MX2-ABH systems, formed by milling over a defined time leads to a formation of well ordered 2D composites of semiconductive MX2 and insulating BN. Even more important, here presented mechanochemical hybridization of MX2 with ABH opens a possibility for simple preparation of potentially interesting MX-based composite materials for energy conversion and storage with ABH acting as a multifunctional intercalator. Thus, here described procedure is a quiescent, low cost, flexible, scalable and ecologically friendly method for formation of compositionally tunable composite 2D materials with numberous potential applicative perspectives, especially in (photo)electrochemical HER catalysis and gas sensing.

Conflicts of interest

There are no conflicts of interest to declare.

Electronic supplementary material

Electronic Supplementary Information (ESI) available: experimental details, with description of milling jars and preparational procedures; PXRD

patterns and derived dependencies; IR spectra; TG-QMS and temperature-dependant IR spectra. See DOI: 10.1039/b000000x/

Acknowledgements

References

[1] F. Bozheyev, Transition metal dichalcogenide thin films for solar hydrogen production, Curr. Op. Electrochem. 34 (2022) 100995. doi:10.1016/j.coelec.2022.100995.

[2] F. Bozheyev, K. Ellmer, Thin film transition metal dichalcogenide photoelectrodes for solar hydrogen evolution: a review, J. Mater. Chem. A 10 (2022) 9327–9347. doi:10.1039/d2ta01108e.

[3] M. Liu, C. Zhang, A. Han, L. Wang, Y. Sun, C. Zhu, R. Li, S. Ye, Modulation of morphology and electronic structure on MoS_2-based electrocatalysts for water splitting, Nano Res. 15 (2022) 6862–6887. doi:10.1007/s12274-022-4297-3.

[4] Y. Lv, P. Chen, J. Foo, J. Zhang, W. Qian, C. Chen, W.-J. Ong, Dimensionality-dependent MoS_2 toward efficient photocatalytic hydrogen evolution: from synthesis to modifications in doping, surface and heterojunction engineering, Mater. Today Nano 18 (2022) 100191. doi:10.1016/j.mtnano.2022.100191.

[5] X. Zhang, S. Hua, L. Lai, Z. Wang, T. Liao, L. He, H. Tang, X. Wan, Strategies to improve electrocatalytic performance of MoS_2-based catalysts for hydrogen evolution reactions, RSC Adv. 12 (2022) 17959–17983. doi:10.1039/d2ra03066g.

[6] O. Yazyev, A. Kis, MoS_2 and semiconductors in the flatland, Mater. Today 18 (2015) 20–30. doi:10.1016/j.mattod.2014.07.005.

[7] Y. Liu, X. Duan, Y. Huang, X. Duan, Two-dimensional transistors beyond graphene and tmdcs, Chem. Soc. Rev. 47 (2018) 6388–6409. doi:10.1039/C8CS00318A.

[8] J. Shim, H.-Y. Park, D.-H. Kang, J.-O. Kim, S.-H. Jo, Y. Park, J.-H. Park, Electronic and optoelectronic devices based on two-dimensional materials: From fabrication to application, Adv. El. Mater. 3 (2017) 1600364. doi:10.1002/aelm.201600364.

[9] W. Chen, X. Gui, L. Yang, H. Zhu, Z. Tang, Wrinkling of two-dimensional materials: methods, properties and applications, Nanoscale Horiz. 4 (2019) 291–320. doi:10.1039/C8NH00112J.

[10] R. Mahlouji, Y. Zhang, M. A. Verheijen, J. P. Hofmann, W. M. M. Kessels, A. A. Sagade, A. A. Bol, On the contact optimization of ald-based MoS_2 fets: Correlation of processing conditions and interface chemistry with device electrical performance, ACS Appl. El. Mater. 3 (2021) 3185–3199. doi:10.1021/acsaelm.1c00379.

[11] S.-J. Choi, I.-D. Kim, Recent developments in 2d nanomaterials for chemiresistive-type gas sensors, El. Mater. Lett. 14 (2018) 221–260. doi:10.1007/s13391-018-0044-z.

[12] A. Sinha, Dhanjai, B. Tan, Y. Huang, H. Zhao, X. Dang, J. Chen, R. Jain, MoS_2 nanostructures for electrochemical sensing of multidisciplinary targets: A review, Trends Anal. Chem. 102 (2018) 75–90. doi:10.1016/j.trac.2018.01.008.

[13] S. Mao, J. Chang, H. Pu, G. Lu, Q. He, H. Zhang, J. Chen, Two-dimensional nanomaterial-based field-effect transistors for chemical and biological sensing, Chem. Soc. Rev. 46 (2017) 6872–6904. doi:10.1039/C6CS00827E.

[14] R. Wadhwa, A. V. Agrawal, M. Kumar, A strategic review of recent progress, prospects and challenges of MoS_2-based photodetectors, J. Phys. D 55 (2021) 063002. doi:10.1088/1361-6463/ac2d60.

[15] E. Singh, P. Singh, K. S. Kim, G. Y. Yeom, H. S. Nalwa, Flexible molybdenum disulfide (MoS_2) atomic layers for wearable electronics and optoelectronics, ACS Appl. Mater. Interf. 11 (2019) 11061–11105. doi:10.1021/acsami.8b19859.

[16] Z. Zheng, T. Zhang, J. Yao, Y. Zhang, J. Xu, G. Yang, Flexible, transparent and ultra-broadband photodetector based on large-area WSe_2 film for wearable devices, Nanotech. 27 (2016) 225501. doi:10.1088/0957-4484/27/22/225501.

[17] N. Li, Q. Wang, C. Shen, Z. Wei, H. Yu, J. Zhao, X. Lu, G. Wang, C. He, L. Xie, J. Zhu, L. Du, R. Yang, D.-X. Shi, G. Zhang, Large-scale flexible and transparent electronics based on monolayer molybdenum disulfide field-effect transistors, Nature El. 3 (2020) 1–7. doi:10.1038/s41928-020-00475-8.

[18] M. Zhu, X. Du, S. Liu, J. Li, Z. Wang, T. Ono, A review of strain sensors based on two-dimensional molybdenum disulfide, J. Mater. Chem. C 9 (2021) 9083–9101. doi:10.1039/D1TC02102H.

[19] T. W. Scharf, S. V. Prasad, Solid lubricants: a review, J. Mater. Sci. 48 (2013) 511–531. doi:10.1007/s10853-012-7038-2.

[20] Z. Zhuang, J. Huang, Y. Li, L. Zhou, L. Mai, The holy grail in platinum-free electrocatalytic hydrogen evolution: Molybdenum-based catalysts and recent advances, ChemElectroChem 6 (2019) 3570–3589. doi:10.1002/celc.201900143.

[21] J. Huang, Y. Jiang, T. An, M. Cao, Increasing the active sites and intrinsic activity of transition metal chalcogenide electrocatalysts for enhanced water splitting, J. Mater. Chem. A 8 (2020) 25465–25498. doi:10.1039/D0TA08802A.

[22] M.-H. Jeong, H.-S. Ra, S.-H. Lee, D.-H. Kwak, J. Ahn, W. S. Yun, J. Lee, W.-S. Chae, D. K. Hwang, J.-S. Lee, Multilayer WSe_2/MoS_2 heterojunction phototransistors through periodically arrayed nanopore structures for bandgap engineering, Adv. Mater. 34 (2022) 2108412. doi:10.1002/adma.202108412.

[23] H. Tang, B. Neupane, S. Neupane, S. Ruan, N. K. Nepal, A. Ruzsinszky, Tunable band gaps and optical absorption properties of bent MoS_2 nanoribbons, Sci. Rep. 12 (2022) 3008. doi:10.1038/s41598-022-06741-3.

[24] C. Backes, T. M. Higgins, A. Kelly, C. Boland, A. Harvey, D. Hanlon, J. N. Coleman, Guidelines for exfoliation, characterization and processing of layered materials produced by liquid exfoliation, Chem. Mater. 29 (2017) 243–255. doi:10.1021/acs.chemmater.6b03335.

[25] J. N. Coleman, M. Lotya, A. O'Neill, S. D. Bergin, P. J. King, U. Khan, K. Young, A. Gaucher, S. De, R. J. Smith, I. V. Shvets, S. K. Arora, G. Stanton, H.-Y. Kim, K. Lee, G. T. Kim, G. S. Duesberg, T. Hallam, J. J. Boland, J. J. Wang, J. F. Donegan, J. C. Grunlan, G. Moriarty, A. Shmeliov, R. J. Nicholls, J. M. Perkins, E. M. Grieveson, K. Theuwissen, D. W. McComb, P. D. Nellist, V. Nicolosi, Two-dimensional nanosheets produced by liquid exfoliation of layered materials, Science 331 (2011) 568–571. doi:10.1126/science.1194975.

[26] V. Nicolosi, M. Chhowalla, M. G. Kanatzidis, M. S. Strano, J. N. Coleman, Liquid exfoliation of layered materials, Science 340 (2013) 1226419. doi:10.1126/science.1226419.

[27] R. J. Smith, P. J. King, M. Lotya, C. Wirtz, U. Khan, S. De, A. O'Neill, G. S. Duesberg, J. C. Grunlan, G. Moriarty, J. Chen, J. Wang, A. I. Minett, V. Nicolosi, J. N. Coleman, Large-scale exfoliation of inorganic layered compounds in aqueous surfactant solutions, Adv. Mater. 23 (2011) 3944–3948. doi:10.1002/adma.201102584.

[28] J. Kim, S. Kwon, D. Cho, B. Kang, H. Kwon, Y. Kim, S. Park, G. Jung, E. Shin, W. Kim, H. Lee, G. Ryu, M. Choi, T. H. Kim, J. Oh, S. Park, S. Kwak, S. Yoon, D. Byun, Z. Lee, C. Lee, Direct exfoliation and dispersion of two-dimensional materials in pure water via temperature control 6 (2015) 8294. doi:10.1038/ncomms9294.

[29] V. Forsberg, R. Zhang, J. Bäckström, C. Dahlström, B. Andres, M. Norgren, M. Andersson, M. Hummelgård, H. Olin, Exfoliated MoS_2 in water without additives, PLOS One 11 (2016) 1–12. doi:10.1371/journal.pone.0154522.

[30] H. Ma, Z. Shen, S. Ben, Understanding the exfoliation and dispersion of MoS_2 nanosheets in pure water, J. Colloid Interf. Sci. 517 (2018) 204 – 212. doi:10.1016/j.jcis.2017.11.013.

[31] D. Saha, V. Patel, P. R. Selvaganapathy, P. Kruse, Facile fabrication of conductive MoS_2 thin films by sonication in hot water and evaluation of their electrocatalytic performance in the hydrogen evolution reaction, Nanoscale Adv. 4 (2022) 125–137. doi:10.1039/D1NA00456E.

[32] W. Zheng, L. Y. S. Lee, Beyond sonication: Advanced exfoliation methods for scalable production of 2d materials, Matter 5 (2022) 515–545. doi:10.1016/j.matt.2021.12.010.

[33] D. Kong, H. Wang, J. J. Cha, M. Pasta, K. J. Koski, J. Yao, Y. Cui, Synthesis of MoS_2 and $MoSe_2$ films with vertically aligned layers, Nano Lett. 13 (2013) 1341–1347. doi:10.1021/nl400258t.

[34] P. P. Tummala, C. Martella, A. Molle, A. Lamperti, Ambient pressure chemical vapor deposition of flat and vertically aligned MoS_2 nanosheets, Nanomater. 12 (2022). doi:10.3390/nano12060973.

[35] J. Ding, Y. Zhou, Y. Li, S. Guo, X. Huang, MoS_2 nanosheet assembling superstructure with a three-dimensional ion accessible site: A new class of bifunctional materials for batteries and electrocatalysis, Chem. Mater. 28 (2016) 2074–2080. doi:10.1021/acs.chemmater.5b04815.

[36] H. Li, C. Tsai, A. L. Koh, L. Cai, A. W. Contryman, A. H. Fragapane, J. Zhao, H. S. Han, H. C. Manoharan, F. Abild-Pedersen, J. K. Nørskov, X. Zheng, Activating and optimizing MoS_2 basal planes for hydrogen evolution through the formation of strained sulphur vacancies, Nature Mater. 15 (2015) 48 – 53. doi:10.1038/nmat4465.

[37] Y. Ouyang, C. Ling, Q. Chen, Z. Wang, L. Shi, J. Wang, Activating inert basal planes of MoS_2 for hydrogen evolution reaction through the formation of different intrinsic defects, Chem. Mater. 28 (2016) 4390–4396. doi:10.1021/acs.chemmater.6b01395.

[38] J. Xu, G. Shao, X. Tang, F. Lv, H. Xiang, C. Jing, S. Liu, S. Dai, Y. Li, J. Luo, Z. Zhou, Frenkel-defected monolayer MoS_2 catalysts for efficient hydrogen evolution, Nature Commun. 13 (2022) 2193. doi:10.1038/s41467-022-29929-7.

[39] X. Liu, X. Jiang, G. Shao, H. Xiang, Z. Li, Y. Jin, Y. Chen, H. Jiang, H. Li, J. Shui, Y. Feng, S. Liu, Activating the electrocatalysis of MoS_2 basal plane for hydrogen evolution via atomic defect configurations, Small 18 (2022) 2200601. doi:10.1002/smll.202200601.

[40] S. Wang, L. Wang, L. Xie, W. Zhao, X. Liu, Z. Zhuang, Y. L. Zhuang, J. Chen, S. Liu, Q. Zhao, Dislocation-strained MoS_2 nanosheets for high-efficiency hydrogen evolution reaction, Nano Res. 15 (2022) 4996–5003. doi:10.1016/j.cej.2021.133592.

[41] B. Hinnemann, P. G. Moses, J. Bonde, K. P. Jørgensen, J. H. Nielsen, S. Horch, I. Chorkendorff, J. K. Nørskov, Biomimetic hydrogen evolution: Mos2 nanoparticles as catalyst for hydrogen evolution, J. Am. Chem. Soc. 127 (2005) 5308–5309. doi:10.1021/ja0504690.

[42] P. Baláž, M. Achimovičová, M. Baláž, P. Billik, Z. Cherkezova-Zheleva, J. M. Criado, F. Delogu, E. Dutková, E. Gaffet, F. J. Gotor, R. Kumar, I. Mitov, T. Rojac, M. Senna, A. Streletskii, K. Wieczorek-Ciurowa, Hallmarks of mechanochemistry: from nanoparticles to technology, Chem. Soc. Rev. 42 (2013) 7571–7637. doi:10.1039/C3CS35468G.

[43] T. F. Jaramillo, K. P. Jørgensen, J. Bonde, J. H. Nielsen, S. Horch, I. Chorkendorff, Identification of active edge sites for electrochemical H_2 evolution from MoS_2 nanocatalysts, Science 317 (2007) 100–102. doi:10.1126/science.1141483.

[44] C. He, Q. Li, X. Zhang, Y. Lu, D. Qiu, Y. Chen, X. Cui, Mechanochemical synthesis of ammonia employing H_2O as the proton source under room temperature and atmospheric pressure, ACS Sust. Chem. Eng. 10 (2022) 746–755. doi:10.1021/acssuschemeng.1c05643.

[45] J.-L. Do, T. Friščić, Mechanochemistry: A force of synthesis, ACS Cent. Sci. 3 (2017) 13–19. doi:10.1021/acscentsci.6b00277.

[46] S. L. James, C. J. Adams, C. Bolm, D. Braga, P. Collier, T. Friščić, F. Grepioni, K. D. M. Harris, G. Hyett, W. Jones, A. Krebs, J. Mack, L. Maini, A. G. Orpen, I. P. Parkin, W. C. Shearouse, J. W. Steed, D. C. Waddell, Mechanochemistry: opportunities for new and cleaner synthesis, Chem. Soc. Rev. 41 (2012) 413–447. doi:10.1039/C1CS15171A.

[47] D. Sun, D. Ye, P. Liu, Y. Tang, J. Guo, L. Wang, H. Wang, MoS_2/graphene nanosheets from commercial bulky MoS_2 and graphite as anode materials for high rate sodium-ion batteries, Adv. En. Mater. 8 (2018) 1702383. doi:10.1002/aenm.201702383.

[48] C. E. Machnicki, F. Fu, L. Jing, P.-Y. Chen, I. Y. Wong, Mechanochemical engineering of 2d materials for multiscale biointerfaces, J. Mater. Chem. B 7 (2019) 6293–6309. doi:10.1039/C9TB01006H.

[49] Y. Zhou, L. Xu, M. Liu, Z. Qi, W. Wang, J. Zhu, S. Chen, K. Yu, Y. Su, B. Ding, L. Qiu, H.-M. Cheng, Viscous solvent-assisted planetary ball milling for the scalable production of large ultrathin two-dimensional materials, ACS NanoAccepted for publication (2022). doi:10.1021/acsnano.1c11097.

[50] N. Biliškov, D. Vojta, L. Kótai, I. M. Szilágyi, D. Hunyadi, T. Pasinszki, S. Flinčec Grgac, A. Borgschulte, A. Züttel, High influence of potassium bromide on thermal decomposition of ammonia borane, J. Phys. Chem. C 120 (2016) 25276–25288. doi:10.1021/acs.jpcc.6b09511.

[51] R. Kumar, A. Karkamkar, M. Bowden, T. Autrey, Solid-state hydrogen rich boron–nitrogen compounds for energy storage, Chem. Soc. Rev. 48 (2019) 5350–5380. doi:10.1039/C9CS00442D.

[52] H. Li, Y. Yan, S. Feng, Y. Chen, H. Fan, Ammonia Borane and Its Applications in the Advanced Energy Technology, J. En. Res. Technol. 143 (2021) 110801. doi:10.1115/1.4049929.

[53] F. Li, Q. Tang, A di-boron pair doped MoS_2 (b2@MoS_2) single-layer shows superior catalytic performance for electrochemical nitrogen activation and reduction, Nanoscale 11 (2019) 18769–18778. doi:10.1039/C9NR06469A.

[54] L. H. Acauan, Y. Zhou, E. Kalfon-Cohen, N. K. Fritz, B. L. Wardle, Multifunctional nanocomposite structural separators for energy storage, Nanoscale 11 (2019) 21964–21973. doi:10.1039/C9NR06954B.

[55] NIST X-ray photoelectron spectroscopy database, NIST standard reference database, NIST. Retrieved Sep. 17, 2022 (2020). doi:10.18434/T4T88K.

[56] L. Liu, Z. Xiong, D. Hu, G. Wu, P. Chen, Production of high quality single- or few-layered graphene by solid exfoliation of graphite in the presence of ammonia borane, Chem. Commun. 49 (2013) 7890–7892. doi:10.1039/C3CC43670E.

[57] A. Jawaid, J. Che, L. F. Drummy, J. Bultman, A. Waite, M.-S. Hsiao, R. A. Vaia, Redox exfoliation of layered transition metal dichalcogenides, ACS Nano 11 (2017) 635–646. doi:10.1021/acsnano.6b06922.

[58] K. Miyoshi, Studies of mechanochemical interactions in the tribological behavior of materials, Surf. Coatings Technol. 43-44 (1990) 799–812. doi:10.1016/0257-8972(90)90022-5.

[59] K. Mohammadtabar, S. J. Eder, P. O. Bedolla, N. Dörr, A. Martini, Reactive molecular dynamics simulations of thermal film growth from di-tert-butyl disulfide on an fe(100) surface, Langmuir 34 (2018) 15681–15688. doi:10.1021/acs.langmuir.8b03170.

[60] T. Xing, S. Mateti, L. Li, F. Ma, A. Du, Y. Gogotsi, Y. Chen, Gas protection of two-dimensional nanomaterials from high-energy impacts, Sci. Rep. 6 (2016) 35532. doi:10.1038/srep35532.

[61] Y. Liang, X. Yuan, W. Zhang, Thermodynamic identification of tungsten borides, Phys. Rev. B 83 (2011) 220102. doi:10.1103/PhysRevB.83.220102.

[62] R. Cao, B. Zhou, C. Jia, X. Zhang, Z. Jiang, Theoretical study of the NO, NO_2, CO, SO_2, and NH_3 adsorptions on multi-diameter single-wall MoS_2 nanotube, J. Phys. D: Appl. Phys. 49 (2015) 045106. doi:10.1088/0022-3727/49/4/045106.

[63] C. J. Zhou, W. H. Yang, Y. P. Wu, W. Lin, H. L. Zhu, Theoretical study of the interaction of electron donor and acceptor molecules with monolayer WS_2, J. Phys. D: Appl. Phys. 48 (2015) 285303. doi:10.1088/0022-3727/48/28/285303.

[64] D. P. Chong, F. Wang, Dehydrogenation of ammonia borane impacts valence and core electrons: A photoemission spectroscopic study, ACS Omega 7 (2022) 35924–35932. doi:10.1021/acsomega.2c04632.

[65] A. Y. S. Eng, A. Ambrosi, Z. Sofer, P. Šimek, M. Pumera, Electrochemistry of transition metal dichalcogenides: Strong dependence on the metal-to-chalcogen composition and exfoliation method, ACS Nano 8 (2014) 12185–12198. doi:10.1021/nn503832j.

[66] J. Bonde, P. G. Moses, T. F. Jaramillo, J. K. N, I. Chorkendorff, Hydrogen evolution on nano-particulate transition metal sulfides, Faraday Discuss. 140 (2009) 219–231. doi:10.1039/B803857K.

[67] X. Chia, A. Ambrosi, Z. Sofer, J. Luxa, M. Pumera, Catalytic and charge transfer properties of transition metal dichalcogenides arising from electrochemical pretreatment, ACS Nano 9 (2015) 5164–5179. doi:10.1021/acsnano.5b00501.

[68] T. Shinagawa, A. T. Garcia-Esparza, K. Takanabe, Insight on Tafel slopes from a microkinetic analysis of aqueous electrocatalysis for energy conversion, Sci. Rep. 5 (May) (2015) 1–21. doi:10.1038/srep13801. URL http://dx.doi.org/10.1038/srep13801